

Hafnium-oxide 3-D Nanofilms via the Anodizing of Al/Hf Metal Layers

Alexander Mozalev, Maria Bendova, Francesc Gispert-Guirado, and Eduard Llobet

Chem. Mater., **Just Accepted Manuscript** • DOI: 10.1021/acs.chemmater.8b00188 • Publication Date (Web): 29 Mar 2018

Downloaded from <http://pubs.acs.org> on March 30, 2018

Just Accepted

“Just Accepted” manuscripts have been peer-reviewed and accepted for publication. They are posted online prior to technical editing, formatting for publication and author proofing. The American Chemical Society provides “Just Accepted” as a service to the research community to expedite the dissemination of scientific material as soon as possible after acceptance. “Just Accepted” manuscripts appear in full in PDF format accompanied by an HTML abstract. “Just Accepted” manuscripts have been fully peer reviewed, but should not be considered the official version of record. They are citable by the Digital Object Identifier (DOI®). “Just Accepted” is an optional service offered to authors. Therefore, the “Just Accepted” Web site may not include all articles that will be published in the journal. After a manuscript is technically edited and formatted, it will be removed from the “Just Accepted” Web site and published as an ASAP article. Note that technical editing may introduce minor changes to the manuscript text and/or graphics which could affect content, and all legal disclaimers and ethical guidelines that apply to the journal pertain. ACS cannot be held responsible for errors or consequences arising from the use of information contained in these “Just Accepted” manuscripts.



Hafnium-oxide 3-D Nanofilms via the Anodizing of Al/Hf Metal layers

Alexander Mozalev,^{*,†} Maria Bendova,[†] Francesc Gispert-Guirado,[‡] Eduard Llobet[§]

[†] CEITEC – Central European Institute of Technology, Brno University of Technology, Purkynova 123, 612 00 Brno, Czech Republic

[‡] SRCiT, University Rovira i Virgili, Av. Paisos Catalans 26, 43007 Tarragona, Spain

[§] MINOS-EMaS, University Rovira i Virgili, Av. Paisos Catalans 26, 43007 Tarragona, Spain

ABSTRACT: Hafnium-oxide films with self-organized nanostructured 3-D architectures and variable dimension (10 to 400 nm) are synthesized via the high-current anodizing of thin aluminum-on-hafnium layers in phosphoric, malonic, and oxalic acid electrolytes. In the approach, the self-organized growth of a porous anodic alumina (PAA) film is immediately followed by the fast PAA-assisted re-anodizing of the hafnium underlayer. The PAA-dissolved films consist of arrays of upright-standing hafnium-oxide nanorods held on the substrate by the tiny needle-like ‘nanoroots’ wide-spread over a continuous hafnium-oxide bottom layer. The roots are amorphous Hf_2O_3 while the rods are amorphous HfO_2 - Hf_2O_3 - Al_2O_3 mixed oxides, the bottom layer being, however, highly textured nanocrystalline HfO_2 . The calculated transport numbers for O^{2-} and $\text{Hf}^{4+(3)+}$ ions are respectively ~ 0.55 and ~ 0.45 , which is a unique situation for anodic hafnium oxide, which normally grows by O^{2-} transport only. Annealing the films in air at 600 °C oxidizes the remaining Hf metal to polycrystalline HfO_2 , still leaving the roots and rods amorphous. The annealing in vacuum results in partial oxide reduction and crystallization of the roots and rods to stable orthorhombic and monoclinic HfO_2 phases. A model of the anodic film growth and solid-state ionic transport is proposed and experimentally justified. Potential applications of the 3-D hafnium-oxide nanofilms are in advanced electronic, photonic, or magnetic micro- and nanodevices.

1. INTRODUCTION

Hafnium dioxide (HfO_2) is a refractory ceramic with excellent electrical and optical properties, which makes it promising for diverse applications.¹ The outstanding chemical stability, large bandgap (5.5–6.0 eV), relatively high dielectric constant (22–25), high breakdown field strength (3.9–6.7 $\text{MV}\cdot\text{cm}^{-1}$), high thermal stability and large heat of formation (271 $\text{kcal}\cdot\text{mol}^{-1}$) make HfO_2 suitable in the field of electroceramics, optics, electronics, magneto-electronics, and optoelectronics.² Exceptionally high values of isothermal compressibility were reported for hafnium dioxide doped with nitrogen. HfO_2 has been identified as one of the most promising materials for the nanoelectronics industry to replace SiO_2 because of its higher dielectric constant and stability in contact with Si.¹ Recently, hybrid structures have been developed integrating HfO_2 with graphene, which combine the versatile functionality of the oxide with the excellent electron transport in graphene, for application in modern high-speed electronics.³ Thin-film HfO_2 ceramics often exhibit multiple crystallographic phases and size-dependent phase transitions among multiple polymorphs. One stable monoclinic phase and several metastable phases, cubic, tetragonal, and orthorhombic, have been identified for HfO_2 . A large band gap of HfO_2 coupled with a low light absorption provides optical transparency over a broad range in the electromagnetic spectrum. HfO_2 dielectrics

can, therefore, operate efficiently down to 220 nm in the ultraviolet and 10 μm in the infrared region.⁴

Over the last decades, efforts have been made to enhance the properties and improve functionality of refractory ceramic films by making the films nanostructured. The growth and manipulation of HfO_2 nanocrystals and nanorods resulted in important applications as optical coatings.² In the Hf–O system, defect concentrations are easier to control when the HfO_2 is formed as nanorods,⁵ such defects can induce ferromagnetism, which has been far more difficult to reproduce in macroscopic HfO_2 . Despite the useful properties and large number of potential applications, the well-controlled preparation of nanostructured hafnium-oxide films with the reproducible chemical composition, crystal structure, and nanomorphology remains a challenge. This is mainly because the optical, electrical, and optoelectronic properties of HfO_2 are highly dependent on the surface/interface structure and chemistry.⁴ HfO_2 ceramics practically available usually present poor crystallinity, irregular particles with broad size distribution and low surface area. Therefore, it is desirable to develop a facile technology for the large-scale synthesis of HfO_2 nanostructures with consideration of versatility and affordability for practical applications. Various deposition methods have been used to synthesize hafnium-oxide-based nanomaterials.^{1,2,3,4} They are generally divided into solution processes (sol-gel, anodizing) and gas-phase processes including both physical (sputter-

ing, PLD) and chemical ((MO)CVD, ALD) vapor deposition methods. Since the early 2000s, nanoporous oxide films grown via direct anodizing of refractory metals on substrates including Hf have been the subject of scientific interest.^{6,7} However, the major difficulty with that technology has been the aggressiveness of the electrolytes combined with the formation of nanochannels or pores in the film volume, which are neither spatially separated nor aligned. There have been no reports on making arrays of regular and spatially separated HfO₂ nanocolumns or rods on a substrate.

In recent years, an alternative approach has been developed to grow 2-D metal-oxide nanostructures (hillocks, rods, or cones) anchored to dielectric or conducting substrates, via smart anodizing of a valve metal bilayer comprising a thin layer of Al superimposed on a different valve metal.⁸ Generally, the overlying aluminum is converted into nanoporous alumina,⁹ and the self-organized growth of the underlying metal oxide occurs locally beneath the alumina pores. Up to now, periodic arrays of metal oxide nanostructures have been successfully grown from the couples including, for example, Ta,⁸ Nb,¹⁰ or W.¹¹ As for the case of Hf, there have been no reports on PAA-assisted anodic formation of hafnium oxides. The major difficulty with this metal is that, first, its anodic oxide grows crystalline, unlike the case of many other valve metals like Ta, Nb, or W, secondly, the transport number for Hf⁴⁺ cation in the oxide is almost zero (0.05).¹² The former results in an intensive oxygen evolution, which may destroy the alumina overlayer, while the latter should be a fundamental obstacle for the oxide to fill up the pores and grow upwards since the oxide with such a low transport number may form at the oxide/metal interface only, i.e. essentially beneath the pores.

In the present work, we have revealed an appropriate combination of the technological, electrical, and electrolytic conditions that allow for nucleation and sustainable growth of PAA-assisted self-organized arrays of HfO₂ nanostructures in such a way that the oxide grows not only at the alumina/metal interface, i.e. under the PAA film, but also inside the pores, filling the pores and getting a shape of pillars or rods, which then can be released via selective PAA dissolution. High-temperature annealing of the anodic films in various atmospheres has helped achieve well-controlled crystallization and phase transition effects. The morphology-composition-structure relationship for the synthesized hafnium-oxide nanostructures has been determined by field-emission scanning (SEM) and transmission electron microscopy (TEM), X-ray photoelectron spectroscopy (XPS), X-ray microdiffraction (XRD), and energy dispersive X-ray (EDX) mapping at the nanoscale. A model of the oxide growth elaborating in 3-D views the details of the surface morphology, oxide/metal interface, and compositional depth profile within the PAA-assisted hafnium-oxide nanofilms is developed.

2. EXPERIMENTAL SECTION

2.1 Sample preparation. A face-side polished Si wafer (*n*-type, 4", 500 μm thick, 4–40 Ω·cm), covered with a 500 nm layer of SiO₂ was used as starting substrate. A layer of Hf, 200 nm thick, followed by a layer of Al, 700 nm thick, were successively deposited on the substrate via the ion-beam sputtering from Hf and Al targets of 99.95% and 99.999% purity, respectively. The anodizing setup was as described elsewhere.¹³ Generally, the anodizing approach involved processing the Al/Hf bilayer in an aqueous acid solution converting the aluminum layer into a PAA film, this being immediately followed by the PAA-assisted anodization of the Hf underlayer at the same cell voltage aiming at formation of an array of hafnium-oxide nanodots under the alumina pores (hereafter the *anodized sample*). After the anodizing, the sample was re-anodized to a higher cell voltage in the same electrolyte to possibly achieve the growth of hafnium-oxide nanorods within the alumina nanopores (hereafter the *re-anodized sample*). Three types of solutions were used as the anodizing electrolytes: 0.2 mol·dm⁻³ phosphoric acid (H₃PO₄), 0.4 mol·dm⁻³ malonic acid (CH₂(COOH)₂), or 0.2 mol·dm⁻³ oxalic acid ((COOH)₂) aqueous solutions to address a range of steady-state anodizing voltages from about 45 to 160 V and to provide the conditions for re-anodizing without a breakdown up to about 400 V. To modify the structural properties of the anodic films, the samples were heated at 600 °C for 5 hours and then slowly cooled down to room temperature in ambient air either at atmospheric pressure (designated as the *air-annealed* films) or at a pressure of 10⁻⁴ Pa (designated as the *vacuum-annealed* films). For microscopic and surface analysis, the alumina overlayer was dissolved partly or completely either in 1 wt.% NaOH aqueous solution (room temperature) or in a selective (towards aluminum) etchant prepared and used as described elsewhere.¹⁴

2.2 Sample characterization. The films were examined by SEM in a TESCAN MIRA II field emission microscope, equipped with an InBeam detector for secondary electrons, without depositing any conducting layer. XPS analysis was carried out with a Kratos Axis Ultra DLD spectrometer using a monochromatic Al Kα source. The X-ray emission energy was 150 W with a 15 kV accelerating voltage focused to a spot of 300 μm × 700 μm. Typical operating pressures were better than 10⁻⁹ Torr. The emitted electrons were detected by a hemispherical analyzer at fixed pass energies of 160 eV for the survey spectra and 20 eV for the high-resolution spectra. The Kratos charge neutralizer system was used for all specimens. The depth profiling was performed using an argon ion beam of 5 kV provided by a standard ion gun with a sample current of 750 nA scanned over a surface window of 2 mm × 2 mm. Each sputter cycle lasted 250 s (surface) or 1000 s (depth). The angle of incidence of the sputtering beam was 45° with respect to the substrate surface. Spectra were analyzed using CasaXPS software version 2.3.16 PR 1.6. Gaussian (Y%)–Lorentzian (X%) profiles, defined in CasaXPS as GL(X), were used for oxide components. For metallic core lines, asymmetry was defined in the form of LA (α, β, and

m), as elaborated elsewhere.¹⁵ A standard Shirley background was used in all fitted spectra. Spectra from all samples have been charge corrected to give the adventitious C 1s spectral component (C–C, C–H) a binding energy of 285.0 eV. The process has an associated error of ± 0.2 eV.¹⁶ The peak-fitting of C 1s spectra was guided by the strategy explained in the Supporting Information with reference to the C 1s spectrum of the unspattered PAA-free re-anodized sample (Figure S1). **XRD analysis** was carried out in a Bruker-AXS D8-Discover diffractometer, equipped with parallel incident beam (Göbel mirror), vertical θ - θ goniometer, XYZ motorized stage, and a General Area Detector Diffraction System (GADDS). An X-ray collimator of 500 μm system allowed the analysis of a mean area represented by an ellipsoid with a constant short axis of 500 μm and a variable long axis of 1500 down to 600 μm . The X-ray diffractometer was operated at 40 kV and 40 mA to generate Cu K_{α} radiation. The GADDS detector was an HI-STAR (multiwire proportional counter of 30 cm \times 30 cm with a 1024 \times 1024 pixel grid) placed at a 15-cm distance from the sample. Three frames (2-D diffractograms) were collected in the reflecting mode covering 20–90° 2θ . The exposition time was 900 s per frame, and the data were γ -integrated to generate the conventional 2θ vs. intensity diffractogram. The experimental diffractograms were fitted with the crystal structure (Rietveld analysis)¹⁷ for the phases identified with the aid of TOPAS 5.0 software. From these fittings, the cell parameters and microstructure (crystallite size and preferred orientation) of the detected phases were determined using the Double Voigt approach.¹⁸ We considered that the samples were free of microstrain as the secondary cause of the peak broadening in order to simplify the refinement. The wt.% of the phases involved was estimated by refining the Rietveld scale factor and applying the corresponding formulas.¹⁹ The instrumental contribution was obtained from a sample of LaB₆ (SRM 660a) analyzed under the same conditions and was considered prior to estimating the microstructure contribution to the peak width. More details of the XRD analysis and relevant interpretations can be found in Supporting Information. Cross sections of the anodic oxide films on SiO₂/Si substrates were examined by **HRTEM-EDX** in an FEI Titan Themis 60-300 transmission electron microscope operated at accelerating voltage of 300 kV. Lamellas with thicknesses of ~ 80 nm were prepared by focused ion beam (FIB) milling in an FEI Helios microscope. Prior to film sectioning, for preventing top-surface damage, the sample surfaces were covered with a layer of Pt, about 600 nm thick, via FIB-assisted deposition. The rough milling was done at 30 keV and the fine polishing was performed at 5 keV. Selected TEM images or their parts were subjected to fast Fourier transform (FFT) analysis using FEI software TEM Imaging & Analysis version 4.14. To obtain the chemical composition of the film sections, EDX analysis was performed on the FIB-cut lamellas using a high-sensitivity FEI Super-X detector by scanning a selected area of the lamella with the 300 kV electron beam and a beam current ~ 1 nA, dwell time 20 μs , pixel size 2 or 4 nm. Quantitative evaluation of the data was performed using

FEI software Velox version 2.2.1. Data integration was performed over selected parts of the film sections within and beneath individual nanorods. The integrated spectra were corrected by empirical background correction, and the semi-empirical Schreiber-Wims ionization cross-section model was used for quantification, which is suitable for metal oxides. All elements present were used for calculation of at% and for making elemental maps, whereas for quantitative analysis of the various parts of the anodic film they were recalculated to obtain Hf+Al+O+P=100 at%. The correct estimation of P was a challenging task due to the overlapping of P K_{α} line with Pt M line. Nevertheless, carefully checking the EDX spectra integrated from different sample parts helped distinguish reliably between the elements (Supporting Information).

3. RESULTS

3.1 Anodizing behavior. It should first be noted that the experiments on anodizing/re-anodizing the Al/Hf bilayer performed in the usual way, that is, at moderate current densities (0.5–10 mA·cm⁻²) all unfortunately resulted in the formation of hafnium-oxide layer beneath the PAA/Hf interface. In other words, the oxide formed via the inward migration of O²⁻ ions and no oxide was formed within the alumina nanopores via outward migration of the cation (Hf⁴⁺), as actually one may expect from the theoretical viewpoint.¹²

As noted in the introduction, these features make the efforts to achieve a sustainable oxide growth of hafnium anodic oxides through the alumina nanopores extremely challenging. Here, after a series of experiments, we have revealed the right conditions of electrical and electrolytic variables to initiate and maintain the pore-assisted growth of anodic oxides on Hf in a wide range of cell voltages without an electrical breakdown and destructive physical defects. The approach is based on applying the high-current mode that has been proposed in previous works by the present authors.^{15,20} Here, we modified the method to anodize an Al/Hf bilayer. As an example, **Figure 1** shows the electrochemical responses during the constant-current anodization of the Al/Hf/SiO₂/Si sample in 0.2 mol·dm⁻³ H₃PO₄. At the commencement of the 200 mA·cm⁻² constant-current polarization, the formation voltage rises, at a rate of about 40 V·s⁻¹ before reaching a maximum of about 180 V, and then decreases gradually until a steady-state value of ~ 160 V is taken up (the end of stage I, Figure 1). During the next stage II, a PAA layer grows until its barrier layer reaches the underlying Hf metal in about 23 s at the given current density and film thickness, then the voltage begins to increase, at an extremely fast rate of ~ 80 V·s⁻¹, to reach a set value of 400 V. At the set point, the power supply is automatically switched into the constant-voltage regime, preventing the oxide from further growth, this being accompanied by a short, 10-second current decay. Despite some current instability during stages I and III caused by the inability of the power supply to precisely maintain such a high current while the voltage is changing so fast and in such a

1 wide range, the voltage-time curve looks quite right for
2 what may be expected for the growth of a PAA film hav-
3 ing a good degree of pore ordering^{15,20} (more comments
4 on the anodizing behavior can be found in the Supporting
5 Information, section S2).

6 The high current flowing through the anodic oxides
7 may cause the formation of amorphous hafnium anodic
8 oxide in the alumina nanopores, provided the transport
9 number for hafnium ions in amorphous HfO₂ is higher
10 than zero, which must be the key condition for the oxide
11 to grow within the pores. Before filling the pores, the
12 growing hafnium oxide must penetrate the alumina barrier
13 layer, which may happen if the transport number of
14 Hf⁴⁺ in Al₂O₃ would also be higher than zero and the haf-
15 nium oxide would form amorphous within the alumina
16 barrier layer. To maintain the high current regime and
17 hence the high field across the growing oxide, the anodiz-
18 ing is immediately followed by re-anodizing, without a
19 current decay between the stages. This is also expected to
20 prevent or weaken the field-assisted crystallization of the
21 oxides and provide the transport-number criterion for
22 further growth of amorphous anodic hafnium oxide inside
23 the pores.

24 From the above consideration, it is highly possible that
25 the failure to grow hafnium-oxide nanorods in the pores
26 via the usual anodization/re-anodization was caused by
27 the prevailing field-assisted crystallization of the whole
28 volume of anodic oxide, in which the transport number
29 for Hf⁴⁺ is almost zero (0.05).¹² As a support for this
30 statement, the voltage-time and current-time responses
31 for conventional anodizing/re-anodizing of the same
32 Al/Hf bilayers in the phosphoric and malonic acid electro-
33 lytes are shown in direct comparison with the high-
34 current anodizing regime in the Supporting Information,
35 section S2, Figures S2 and S3.

36 **3.2 Film morphology.** SEM images in Figure 2a–d
37 show an anodic film derived from an Al/Hf bilayer on the
38 SiO₂/Si wafer generated during stage I in Figure 1 (the
39 anodized sample), before and after selectively dissolving
40 the alumina layer. An array of nanosized protrusions is
41 revealed, presumably of hafnium oxide, penetrating the
42 alumina barrier layer (Figure 2a) and free-standing after
43 dissolving the PAA overlayer (Figure 2b and c). Each pro-
44 trusion consists of two parts – the upper one that grows
45 above the Al₂O₃/Hf interface, which penetrates the alu-
46 mina barrier layer, and the lower one below the interface,
47 which forms as a local concave depression in the hafnium
48 layer. Above the surface of the hafnium film, there is no
49 sign of aluminum, which might remain at the stage of
50 anodizing.⁸ An important feature is that the protrusions
51 are not dense but composed of a number of tiny ‘nanoneedles’
52 rising up from the general level of hafnium metal,
53 being well-spread at their bottoms but localized within an
54 area that fits the size of corresponding alumina cells.
55 Likely, the gaps between the neighboring collections of
56 needles are already passivated by a thin layer of hafnium
57 anodic oxide, which forms yet before the potential begins
58 to increase. The image in Figure 2d generated from an
59 area close to the protecting ring of the anodizing bath

may give an idea of how the needles are developing from
the moment when the alumina barrier layer is just touch-
ing the underlying hafnium until the stage at which the
formation of needles is complete and the voltage is about
to go up.

Figure 2e–h shows the cross-fractures and surfaces of
the *re-anodized sample*, i.e. processed to the end of stage
IV in Figure 1. Thus, re-anodizing the sample to 400 V
results in lengthening the oxide protrusions along the
alumina nanopores in the form of vertically aligned (per-
pendicular to the substrate) nanorods, all being of nearly
the same height of 400 nm, an average diameter of
100 nm, and a population density of 7·10⁸ cm⁻². A relatively
uniform grey band is evident within the film fracture
between the remaining Hf metal and the PAA layer (Fig-
ure 2e). Presumably, the band and rods represent hafni-
um-oxide-containing regions formed over the residual
hafnium layer. Thus, two layers are distinguished in the
re-anodized samples: an upper, structured layer compris-
ing the nanoroots holding the nanorods that grow above
the alumina barrier layer (in the pores) and a lower, con-
tinuous solid layer of about 100 nm thickness that forms
between the structured layer and the residual hafnium
metal. Experiments with the oxalic and malonic acid elec-
trolytes also revealed the principal possibility to grow
PAA-assisted hafnium-oxide nanostructures, being com-
posed of nanorods of relatively smaller diameters (40 and
80 nm respectively), as one may expect due to the volt-
age-related changes in pore sizes in the corresponding
PAA films.^{21,22} Selected SEM images of the films derived
from an Al/Hf metal bilayer anodized/re-anodized in
0.2 mol·dm⁻³ oxalic acid aqueous solution at 50/400 V are
shown in Figure 3. As seen, the rods synthesized in the
oxalic acid have obviously denser bases, created by
merged nanoneedles. Moreover, the length/diameter ratio
for the oxalic-acid nanorods is almost 10, whereas that for
the phosphoric-acid-made nanorods is smaller than 4.
Based mostly on SEM observations of the phosphoric-
acid-made nanofilms, a scheme was developed with a
computer-aided graphic program elaborating the main
stages of film nucleation and growth (Figure 4).

3.3 Chemical composition. The phosphoric-acid-
made samples have been selected for detailed analytical
investigation described in the following sections. First,
XPS analysis was applied to the PAA-free and PAA-half-
etched *anodized* (Figure 4d’), *re-anodized* (Figure 4e’),
vacuum-annealed, and *air-annealed* films. A bare Hf layer
was used as a reference surface. The presence of carbon,
hafnium, oxygen, and phosphorous was identified in the
survey spectra of all not sputter-cleaned surfaces. Narrow-
scan C 1s, Hf 4f, O 1s, Al 2p, and P 2p spectra were collect-
ed to analyze the core levels of the above elements.

From the relevant literature,^{23,24,25,26,27} charging during
photon or electron irradiation of an HfO₂ film can make it
difficult to determine the binding energies and/or the
chemical states accurately, which may lead to incorrect
peak assignments. For example, the binding energy of the
Hf 4f_{7/2} levels of a thick HfO₂ film has been estimated as
17.3 and 17.4 eV,^{26,27} differing by about 1 eV from the other

reported values.²³ Additional confusion may arise from incorrect assignment of the surface and the bulk states.²⁷ That is why we began with analyzing by XPS a reference hafnium film derived from the Al/Hf bilayer after selectively dissolving away the Al layer. Due to exposure to air before the analysis, the metal surface was expected to receive a thin (few nanometers) air-formed oxide film. A narrow scan Hf 4f spectrum of the *Hf metal film* is shown in **Figure 5a**. The Hf 4f region can be fitted with two spin-orbit doublets, each with 1.68 eV separation, with the corresponding $4f_{7/2}$ binding energies at 14.35 and 18.15 eV. The first doublet has relatively narrow peaks, with full width at half maximum (FWHM) of 0.4 eV and clearly asymmetric lineshape, which is well fitted with LA(1,2,5) and can be assigned to the Hf^0 metal. The second doublet exhibits larger width (1.25 eV) and symmetric lineshape, and can accordingly be assigned to the fully oxidized Hf^{IV} . The 3.8 eV shift for HfO_2 is in agreement with the previously reported XPS values. No sign of presence of hafnium suboxides is found in the air-formed oxide on the hafnium metal. Based on this analysis and with reference to the literature reports, for all Hf 4f spectra acquired in this work, the Hf $4f_{5/2}$ peak for each species was constrained to be at a fixed energy increment of 1.68 eV above the Hf $4f_{7/2}$ peak, and the peak intensity ratio was fixed to 4:3. The FWHM's for Hf^{IV} $4f_{7/2}$ and $4f_{5/2}$ components were set slightly narrower than those for the Hf^{IV} 4f doublets with $n < 4$ as the structure of hafnium suboxides is thought to be relatively loosely ordered.^{27,28}

Figure 5b shows Hf 4f spectrum of the *anodized sample* (sketched in the inset) after selective PAA removal. Two doublets with symmetric lineshape are used to reproduce the Hf 4f spectrum, with the $4f_{7/2}$ binding energies of 16.9 and 18.3 eV. The higher-energy doublet, having narrower FWHM (1.35 eV) is assigned to the Hf^{IV} oxidation state (HfO_2). The second (dominating) doublet is shifted to -1.4 eV from the higher-energy component (Hf^{IV}) exhibits relatively larger width (1.45 eV) and can accordingly be assigned to a suboxide with Hf^{n+} , where $n < 4$, most likely Hf^{3+} .²³ Neither Al nor Hf metals are detected on the anodized sample surface. This means that the Hf metal surrounding the hafnium-oxide protrusions is covered by a layer of anodic oxide that forms already during the anodizing stage. This feature discriminates the PAA-assisted hafnium-oxide nanostructured surfaces from PAA-assisted oxides on W and Nb.^{10,15}

The Hf 4f spectra of the *re-anodized half-etched* (Figure 5c), *re-anodized PAA-free* (Figure 5d), and *re-anodized rod-free* (Figure 5e) samples are all well reproduced by the two doublets having symmetric lineshapes and associated with photoelectrons emitted from Hf^{IV} and Hf^{3+} oxidation states. The values of binding energy for the Hf^{IV} $4f_{7/2}$ feature ranging 18.3 to 18.1 eV and the chemical shift of 1.0 eV for the suboxide component are generally in agreement with the previously reported XPS values for hafnium oxides.^{25,26,27} The differences between the above spectra are in the percentage of the spectral components for each spectrum. From comparison of the three spectra, the atomic concentration of Hf^{3+} , presumably in the form of

Hf_2O_3 , is minimal in the rod-free sample (24.5 at%), rises up in the rods (44.5 at%), and reaches a maximum in the PAA-free sample (82.5 at%). It should be noted that the rod-free surface examined by XPS was merely the *bottom oxide layer*, from which the rods and roots had been removed by ultrasonic treatment, and in case of the PAA-free samples the highest contribution to the signal originates from the roots. Therefore, the relative content of Hf_2O_3 in the anodic film rises up in the order: bottom oxide ($\sim HfO_2$) \rightarrow rods (mixed HfO_2 - Hf_2O_3) \rightarrow roots ($\sim Hf_2O_3$). The roots being almost fully composed of Hf_2O_3 are also the case of the anodized film (88.0 at% of Hf^{3+}). Table S2 (Supporting Information) summarizes the binding energies for the Hf $4f_{7/2}$ level, FWHM values, atomic concentrations of spectral components, and peak assignments for all the samples prepared and XPS-examined in this study.

Figure 5f shows Hf 4f spectrum of the *vacuum-annealed* sample, sketched in the inset. The Hf 4f region is reproduced by three spin-orbit doublets, with the corresponding $4f_{7/2}$ binding energies at 18.3, 17.3, and 14.65 eV. Similarly to the above interpretation, the two higher-energy doublets are assigned to the full (Hf^{IV} , 23.5 at%) oxidation state and a suboxide (Hf^{3+} , 69.0 at%), respectively. The lower-energy doublet has relatively narrow linewidth (0.95 eV) and asymmetric lineshape (LA(1,2,5)) and can be assigned to the Hf^0 (metal, 7.5 at%). Notably, among the nanostructured samples prepared in this study, the vacuum-annealed PAA-free surface has been the only case that revealed the presence of hafnium metal, which obviously results from partial reduction of the oxide due to the heating in the oxygen deficient atmosphere. As the vacuum-annealed PAA-half-etched surface had no metallic Hf (spectrum not shown), the hafnium metal must be present in the roots of the vacuum-annealed film. As at the rod tops the content of Hf^{3+} (45.0 at%) is relatively lower than that at the corresponding PAA-free surface (69.0 at%), it is assumed that the relative concentration of Hf_2O_3 in the vacuum-annealed sample increases from the rods (mixed HfO_2 - Hf_2O_3) to roots ($\sim Hf_2O_3$ + a portion of metallic Hf).

In the *air-annealed sample* (Figure 5g), no hafnium metal is found at the surface, and the atomic concentrations of the full oxide and suboxide change drastically, the Hf^{IV} portion increasing and dominating the HfO_2 - HfO_x composition (57.0 at%). Obviously, oxidation of a portion of the Hf_2O_3 suboxide occurs during the heating in air, leading to a higher amount of HfO_2 . The lower-energy doublet distanced from the main component to only -0.75 eV cannot be reliably assigned to Hf^{3+} oxidation state but more realistically to Hf^{n+} where n -value is lower than 4 but higher than 3. This may be due to the formation of mixed Hf_2O_3 - HfO_2 containing oxygen vacancies that remain after the annealing.

Further, the presence of Al_2O_3 is noticed in all the PAA-free samples, including the roots of the anodized sample (Figure 4d'). As an example, the Al 2p spectrum of the re-anodized sample (inset of Figure 5h) is well reproduced by a singlet with a binding energy of 74.6 eV, which is

associated with Al_2O_3 . From the quantitative comparison of the Hf 4f and Al 2p spectra (assuming $\text{at}(\text{Hf}+\text{Al}) = 100\%$), the concentration of Al^{3+} at the surface of nanorods and roots together (Figure 4e') is estimated to be 22 at%, while that for the anodized sample (merely the roots, Figure 4d') is only 4 at%.

Atomic concentration profiles for the Hf 4f (separately in metal and oxide), Al 2p (in oxide), O 1s, P 2p, and Si 2p for the PAA-free *re-anodized* and *anodized* samples are shown respectively in Figure 5i and j, along with the sketches of both samples modified by the Ar ion beam (corresponding SEM views are displayed in the Supporting Information, Figure S4 and S5). An amount of adventitious carbon and minor concentration of Si were detected on the unspattered surfaces. The Si signal vanished soon after beginning the sputtering and appeared again when the SiO_2 substrate became exposed to the X-ray beam. In the re-anodized sample, the alumina content first increased with sputter-cleaning the surface but then soon began to decrease, lasting however rather long in the profile. The alumina line appeared to be substantially shorter in the anodized sample, the comparative Al 2p profiles for the two samples are shown in Figure 5k. In both cases, when the alumina signal vanished the hafnium-oxide content reached its maximum. From comparison of the sputter-etched films in Figure S4 (Supporting Information), the depth of alumina incorporation in the oxide nanorods is estimated to be ~ 25 nm. The suggestion that the two oxides mix in the outer film layer is further supported by the analysis of the O 1s-Hf 4s spectrum of the Ar-ion sputter-cleaned surface of the re-anodized sample, shown in Figure 5h. Although the exact binding energy for the Hf 4s peak is not obvious,²⁵ the most intensive peak at 530.8 eV is thought to be mainly due to the oxygen species O^{2-} in HfO_2 while the smaller peak at 531.9 eV is assigned to O^{2-} species bonded in Al_2O_3 . The higher-energy O 1s peak component is likely due to the hydroxylated part of the Al_2O_3 portion of the rod material. The P 2p line lasted even longer than the Al 2p signal until the nanorods were largely sputtered away by the Ar-ion beam. Obviously, while the carbon and silicon species are present only in the outermost layer of organic contamination, the phosphorus-containing impurities are incorporated into the nanorods and also located in the vicinity of the alumina barrier layer and even under (further details of the phosphorus distribution will be revealed in section 3.5).

Conclusively, the XPS analysis shows that the nanorods contain HfO_2 and Hf_2O_3 in comparable concentrations and the nanoroots are mostly Hf_2O_3 , whereas the bottom oxide (at least its upper layer) is mostly HfO_2 . The air annealing increases the portion of HfO_2 in the rods, up to 57.0 at% of Hf^{4+} at the surface of the re-anodized sample, unlike the case of annealing in vacuum, which reduces the oxides in the film and gives rise to metallic Hf in the roots (more support for this statement will be presented in section 3.5). The Al_2O_3 is mostly located in the outer layer of the oxide nanorods, being mixed with hafnium oxide to a depth of ~ 25 nm, likely at molecular level with-

out complex oxide formation.²⁹ A much smaller amount of alumina is found within the roots. It is not yet obvious what hafnium ions (chemical state) compose the inner portion of the bottom oxide and the inner part of the rods. Neither the crystal structure of the material may be determined by XPS analysis. Both issues will be addressed in sections 3.4 and 3.5.

3.4 Crystal structure. Figure 6 shows the recorded, calculated, and difference diffractograms of the anodized, re-anodized, vacuum-, and air-annealed samples in the range of $20\text{--}90^\circ$ 2θ angles. The crystal structures for each phase present in the films were found in the ICSD database (FIZ, 2015), the main refined parameters and details of the XRD line profile and quantitative phase analysis are available in Table S3 (Supporting Information). The diffractogram of the *anodized* sample (Figure 6a) is interpreted by the presence of metallic Hf (hexagonal, space group $\text{P6}_3/\text{mmc}$) and HfO_2 (monoclinic, space group $\text{P}2_1/\text{c}$) phases, hereafter *h*-Hf and *m*- HfO_2 , respectively. The relative amount of the metallic phase, estimated by the Rietveld method, is about 73 wt%. Apparently, the *h*-Hf phase is associated with a portion of hafnium metal (from the initial Al/Hf bilayer) that remains unoxidized after completing the anodizing process. It reveals the presence of two preferential crystallographic orientations (see Supporting Information for details): the favored $\langle 001 \rangle$ direction and less preferred $\langle 100 \rangle$ direction. This is associated with the presence of two well-recognized textured populations of *h*-Hf nanocrystallites in the sputter-deposited hafnium film. The *m*- HfO_2 phase grows also textured, preferentially along $\langle 111 \rangle$ direction as noticed by the high intensity of hhh peaks and the low March-Dollase index^{30,31} (PO_{111} : 0.17). The microstructures of *h*-Hf and *m*- HfO_2 phases revealed the crystallite sizes of 11.7 and 19.9 nm, respectively. As the size of the *m*- HfO_2 crystallites is bigger than the diameter of the roots (~ 10 nm), they are probably situated in the bottom oxide only.

For the *re-anodized* sample (Figure 6b), the detected phases are *h*-Hf (30 wt%), *m*- HfO_2 (47 wt%), and orthorhombic HfO_2 , space group Pbca (23 wt%) – hereafter *o*- HfO_2 , identified through a set of low intensity broad peaks. Thus, the re-anodizing process results in reducing the amount of the metal and increasing the portion of oxide, present in the form of the dominating *m*- HfO_2 phase and the minor *o*- HfO_2 phase. It is worth noticing that both the microstructure and texture of the remaining Hf metal and of the enlarged portion of the *m*- HfO_2 remain practically unchanged after the re-anodization. The *o*- HfO_2 develops with a smaller crystallite size (6.4 nm) and grows in a $\langle 210 \rangle$ preferred direction.

The anodized and re-anodized films were XRD investigated also after the roots and nanorods had been removed from the film surfaces via an ultrasonic vibration treatment (diffractograms not shown) so that only the bottom oxide layers remained. Notably, the obtained diffractograms were practically identical to those recorded before the ultrasonic treatment for the two samples. This implies that the crystalline HfO_2 phases identified in the two PAA-free samples (Figure 6a and b) are located merely

1 within the bottom oxide, being present neither in the
2 roots nor in the rods.

3 The diffractograms for the *air-annealed* sample are
4 shown in Figure 6c. The metallic Hf is almost fully
5 consumed (2.5 wt%), the *m*-HfO₂ being most abundant
6 (93 wt%), while the *o*-HfO₂ is present in a substantially
7 smaller amount (4 wt%). Interpretation of the resulting
8 diffractogram is less certain because of the low X-ray
9 scattering power of the *m*-HfO₂. However, it is seen that
10 the texture of the *m*-HfO₂ phase changes with the anneal-
11 ing to a more preferred $\langle 10\bar{1}\rangle$ orientation instead of the
12 $\langle 111\rangle$ one, being however relatively less orientated ($PO_{10\bar{1}}$:
13 0.52) than before the annealing (PO_m : 0.19). Thus, it may
14 be concluded that the annealing in air results not only in
15 nearly full oxidation of the Hf metal but also in re-
16 texturing of the *m*-HfO₂ phase and in the presence of
17 substantially smaller *m*-HfO₂ nanocrystallites (7.7 nm)
18 compared with those of the re-anodized sample (16.5 nm).
19 Interestingly, similarly to the re-anodized film, removing
20 the nanorods and roots by ultrasonic vibration does not
21 lead to any change of the diffractogram (not shown),
22 meaning again that only the bottom oxide is crystalline
23 and the upper part of the film remains amorphous, in
24 spite of the high heating temperature, at which hafnium
25 oxide may be expected to crystallize.¹ The smaller crystal-
26 lite size could be a result of the difficulty in self-ordering
27 of the new portion of thermal HfO₂ grown below the
28 original anodic bottom oxide and in recrystallization of
29 the anodic HfO₂.

30 The phases identified in the *vacuum-annealed* sample
31 (Figure 6d) are the same as those in the re-anodized film
32 but they appear in different proportions. A seeming
33 change in the degree of hafnium oxidation is noticed
34 through the reduction of a portion of metallic Hf to 14
35 wt% relative to 30 wt% in the re-anodized sample,
36 accompanied by an increase in the percentage of the *m*-
37 HfO₂ phase. Such a paradoxical drop in the Hf/HfO₂ ratio
38 under the vacuum annealing conditions, when the
39 remaining Hf metal is not expected to oxidize, may only
40 be explained by assuming that an extra portion of amor-
41 phous hafnium oxide composing the film (nanorods and
42 roots) crystallizes during the heating in vacuum. This
43 means that the rods and/or nanoroots of the vacuum-
44 annealed sample are crystalline, unlike the case of any
45 other sample examined in this study. This is also support-
46 ed by measuring a rod-free vacuum-annealed sample (not
47 shown), showing substantial differences in the diffracto-
48 gram. The microstructure and texture of the *m*-HfO₂
49 phase in the vacuum-annealed sample are quite similar to
50 those of the re-anodized sample. The crystallite size is 17
51 vs. 16.5 nm for the two films and the main preferential
52 orientation remains the $\langle 111\rangle$ direction, whereas the less
53 preferred direction changes to $\langle 10\bar{2}\rangle$, which is structur-
54 ally very close to the $\langle 10\bar{1}\rangle$ direction associated with
55 both the re-anodized and air-annealed samples. Another
56 important feature of the vacuum-annealed sample is that
57 there is no indication of any Hf₂O₃ phase, which means
58 that the amorphous hafnium suboxide composing the

roots and rods (well detected by XPS) does not crystallize
during the 600 °C vacuum annealing.

In summary, it is clear now that the rods and roots
grow amorphous during the PAA-assisted re-anodizing
whereas the bottom oxide forms crystalline, consisting of
m-HfO₂ and *o*-HfO₂ stable phases. The annealing in air
leads to a thermal oxidation of the metallic Hf but does
not crystallize the amorphous rods and roots, which is,
however, the case of the vacuum annealing treatment.

3.5 The 'hidden' nanostructure and composition.
The SEM, XPS, and XRD analysis results were finally
complemented by TEM imaging of cross sections and
relevant EDX analysis of the re-anodized, vacuum- and
air-annealed samples. Selected TEM images of a FIB-cut
lamella prepared from the re-anodized sample are shown
in Figure 7. The ~100 nm thick bottom oxide layer and
the ~400 nm long nanorods together with the supporting
nanoroots are clearly distinguished. Besides, the following
features are observed: (1) tiny bubbles (or voids) within
the roots, less than 10 nm in diameter (Figure 7a and b);
(2) the amorphous nature of both the rods and roots (Fig-
ure 7c and d); (3) the bottom oxide layer is composed of
densely packed nanocrystallites, about 15–20 nm in size
(Figure 7c and e). The FFT function applied to the select-
ed parts of the TEM image in Figure 7c confirms the
amorphous nature of the oxide nanoroots and the poly-
crystalline structure of the bottom oxide layer (Figure 7d
and e). The high-resolution TEM image taken across the
border between the amorphous roots and crystalline bot-
tom oxide is shown in Figure 7f, where the crystalline
patterns are clearly seen beneath the border. The amor-
phous nature of the roots was also observed in the case of
the air-annealed sample, which was not the case of the
vacuum-annealed sample (not shown). This finding com-
plements well the XRD results.

To reveal the distribution of chemical elements and
gain an insight into the stoichiometry of hafnium oxide in
the different sample parts, TEM-EDX measurements were
carried out with the lamellas prepared from the re-
anodized (not annealed), vacuum-annealed, and air-
annealed samples. A TEM image of a fragment of the re-
anodized sample is shown in Figure 8a. The EDX data of
the three samples were evaluated in order to obtain ele-
mental maps of Hf, O, Al, and P and to integrate the maps
over the selected areas or lines to obtain chemical compo-
sition in the different sample parts (as marked in Figure
8a). Basically, the analysis reveals the presence of Hf, Al,
O, and P in the anodic film, Si in the substrate, and Pt,
Ga, and C as an outside contamination. The TEM image
of the measured place and the corresponding elemental
maps of selected elements for the *re-anodized* sample are
shown in Figure 8a–e. The Hf and O maps show well the
presence of unoxidized Hf metal over the SiO₂ layer, fol-
lowed by a continuous stripe of HfO_x bottom layer. HfO_x
protrusions into the alumina barrier layer and further into
the pores, being respectively the roots and rods, are also
clearly identified in the Hf map and seen in the Al map as
the areas with a lower Al concentration. Aluminum, as
expected, is detected above the original Al/Hf interface

only, i.e. within the anodic alumina film. We do not show the elemental maps of the vacuum- and air-annealed films since they did not reveal any clear differences except a thicker bottom oxide and a much thinner Hf metal layer in the air-annealed nanofilm. Instead, the combined element maps of the re-anodized and air-annealed samples are added as Figure 8f and g for comparison. It is well seen that the thickness of the bottom oxide increases substantially in the air-annealed film, thus leaving a very thin strip of the Hf metal underneath.

As the anodizing and re-anodizing were performed in an H_3PO_4 electrolyte, one may expect incorporation of phosphorus-containing species into the alumina cell walls and possibly into the HfO_x film. Indeed, a careful check of the P map (Figure 8e) and of integrated EDX spectra from the different lamella's parts reveal that phosphorus is present in the outer part of the alumina cell walls, the P:Al ratio being 0.04, whereas a substantially lower amount of phosphorus is detected in the inner part of the alumina cell walls (P:Al < 0.01), both findings being in agreement with what is known about the alumina cell wall composition.³² Besides, a considerable amount of phosphorus is detected in an upper part of the bottom oxide layer, located right beneath the collections of nanoroots, as marked in Figure 8e. The lower parts of the bottom oxide do not show any P (as seen in the integrated EDX spectra), although the elemental map reveals its low content (Figure 8e), which is, however, an artifact of program-based EDX evaluation caused by an overlap of the P $K\alpha$ line with the Pt M line. Quantitative evaluation (described later in the text) of the lower part of bottom oxide was therefore performed with P content approaching 0 at%.

The quantitative analysis of the three samples was performed for the following sample parts: (1) rods, (2) roots, (3) upper part of the bottom oxide, (4) lower part of the bottom oxide, and (5) remaining Hf metal, as pointed out in Figure 8a. The objective was to reveal, additionally to the XPS analysis, how the oxidation state of Hf ions changes within the anodic film. Taking into account the presence of phosphorus in the alumina, in the upper part of the bottom HfO_x layer, and presumably also in the nanoroots and rods, the quantitative evaluation of the data was adjusted by assuming the following coordination for the aluminum and hafnium oxides:

- stoichiometric $\text{Al}^{3+}\text{O}_x(\text{PO}_4)_y$ compound, where $y = \text{P:Al}$ ratio; $x = 1.5 - 0.5y$

- substoichiometric $\text{Hf}^{n+}\text{O}_x(\text{PO}_4)_y$ compound, where n is the oxidation state of Hf ions

First, the composition of the P-containing alumina was obtained from the Hf-free parts of the alumina portion, thus giving the value of y for alumina. Next, a mixture of alumina and hafnia over the roots and rods (with at% of Hf being between 5 and 15 and the Hf:Al atomic ratio between 0.14 and 0.6) could be easily distinguished since we know how much O and P belong to the $\text{Al}^{3+}\text{O}_x(\text{PO}_4)_y$ compound (with the known x and y), surrounding the Hf-based oxide, therefore the remaining O and P will be from

the $\text{Hf}^{n+}\text{O}_x(\text{PO}_4)_y$ compound of an unknown composition. This consideration gives the values of x and y of the Hf oxide and, more importantly, reveals the value of n , which is the wanted oxidation state of Hf ions. **Table 1** summarizes the results of estimation of n - and y -values in the $\text{Hf}^{n+}\text{O}_x(\text{PO}_4)_y$ compound for the different sample parts in the three samples. From the table, in the re-anodized film, the n -value is highest in the bottom oxide (3.5), falls inside the rods to 3.1, decreasing even further inside the roots (2.9). This finding well supports the XPS analysis results, thus ultimately confirming that the highest amount of hafnium suboxide ($\text{Hf}^{\beta+}$) is located in the needle-like nanoroots, which develop in the alumina barrier layer (Figure 2). From the analysis of the Hf 4f XP spectrum of the PAA-free re-anodized sample (Figure 5d), the content of $\text{Hf}^{\beta+}$ is ~90 at% in the roots (when considering the half-etched analog, Figure 5c), which is translated to n -value of 3.1 ($n = 3 \times 0.9 + 4 \times 0.1$), which is quite close to n -value determined by the TEM-EDX analysis (2.9). As for the bottom oxide layer, which is composed of polycrystalline HfO_2 (as revealed by XRD and TEM), it may be that traces of unoxidized Hf metal are present inside the bottom oxide layer due to the ultrafast re-anodizing. If this is the case, the presence of such metal nanoinclusions, not seen in the TEM images, may result in relatively lowering the EDX-obtained n -value within the HfO_2 bottom layer, from the expected 4 to calculated 3.5.

The oxidation state of Hf changes considerably due to the annealing. The heating in vacuum leads to a substantial decrease in n -value within the roots and bottom oxide to 2.1 and 2.7 respectively, while not affecting the nanorods. Besides, the oxygen content rises up in the remaining hafnium metal. This is likely to result from the reduction of hafnium oxide. The XPS Hf 4f spectrum shows even the presence of Hf metal in the PAA-free vacuum-annealed sample (Figure 5f), which originates from the roots, as further confirmed by the TEM-EDX analysis. Unlike the vacuum annealing, the heating in air increases n -value of the oxide composing the roots up to 4.1 (practically stoichiometric HfO_2) while the rods and bottom oxide layer become relatively more reduced ($n = 2.1$ and 2.4 respectively). Now there is no doubt that the increase in the Hf^{n+} portion in the Hf 4f spectrum of the air-annealed PAA-free sample (Figure 5g) is merely due to the signal coming out from the oxide nanoroots.

Another feature well revealed by the TEM-EDX analysis is the distribution of phosphorus within the hafnium-oxide nanostructures. The calculated y -values for the different parts of the three films (Table 1) show that the highest content of P in the Hf-based oxide is present in the roots (0.30), decreasing slightly in the nanorods (0.24) and becoming even lower in the upper part of the bottom oxide (0.14). At the first sight, this order contradicts the look of the P-map in Figure 8e. The reason is that the map presents the overall concentration of P, which in the upper part of the film is located not only in the Hf-based oxide but mostly in the alumina. The semispherical inner profile of phosphorus species partly penetrating in the bottom oxide layer (clearly seen on the P-map in Figure

8e) may have developed due to negatively charged electrolyte anions or their derivatives, most likely PO_4^{3-} , migrating inwards at a slower rate relative to the O^{2-} ions mainly during the anodizing stage II (Figure 1) and to some extent further during the re-anodizing stages III and IV (Figure 1).⁸ Taking into account the polycrystalline nature of the bottom oxide, it is suggested that the phosphate is present in phosphate-rich amorphous regions that form along the boundaries of the HfO_2 nanograins.

From the SEM, XPS, XRD, and TEM-EDX results and their interpretation it is strongly anticipated that the 3-D nanomorphology, complex and graded chemical composition, diversity in the Hf ion oxidation states and HfO_2 crystal structure within the differently prepared and treated hafnium-oxide nanofilms are the factors that may impact, in a certain way, the electron transport phenomena in the films, giving rise to dielectric, semiconducting, or specifically combined properties and result in diverse functionalities. This will be the subject of future works.

4. DISCUSSION

4.1 Model of Film Growth. Combining the finding of SEM, XPS, XRD, and TEM-EDX analyses and with reference to relevant literature in the field,^{10,12,15,33,34} we have developed a model of nucleation and growth of PAA-assisted hafnium-oxide nanostructures, sketched in **Figure 9**. During compact anodizing of a layer of aluminum superimposed on a layer of another valve metal, randomly occurring finger-like regions of the underlying oxide may develop and penetrate the upper alumina if the lower anodic oxide is less resistive than the overlying alumina, which is the case of Al/Ta, Al/Mo, or Al/Nb bilayers.^{33-35,36,37} The ionic transport and anodic oxide growth become far more systematic when the above-mentioned couples are anodized in electrolytes for porous alumina formation: an array of nanosized anodic oxide hillocks grows within the alumina barrier layer, as reported in the previous works.^{8,10,11} The resistivity ‘criterion’ can be applied only for systems where the anodic oxides of the deposited metal layer and substrate are both amorphous. If the lower oxide layer grows crystalline, like in case of an Al/Zr bilayer,³⁴ despite the outer anodic Al_2O_3 being more ionically resistive, nanofingers of the lower oxide layer *do not develop* into the outer Al_2O_3 layer, so that the anodic alumina remains fully superimposed over the subsequently formed anodic oxide of zirconium or hafnium.¹² Concerning the present case of PAA-assisted anodization of hafnium, what may be readily expected is a situation when the hafnium oxide forms fully under the alumina barrier layer, without penetrating or mixing with the upper alumina. Actually, this happened when we first tried to process the Al/Hf bilayer generally following the procedure reported for aluminum superimposed on the other valve metals, for instance Nb.¹⁰ However, after a series of experiments involving the wide variation of anodizing variables, we were able to ‘tune’ the oxidation behavior of the Al/Hf metal layers in such a way that nanoneedles of hafnium oxide begin to form immediately when the alumina barrier layer is touching the hafnium

layer (Figure 9a and b), and they keep growing pushing their way through the overlying alumina barrier layer over the anodizing stage (Figure 9c), resulting in the partial inversion of the orders of metal and oxygen. The portion of the oxide that forms beneath the $\text{Al}_2\text{O}_3/\text{Hf}$ interface is *polycrystalline* and largely composed of HfO_2 while the needles that protrude above the interface are *amorphous* and mostly, if not exclusively, composed of Hf_2O_3 . The situation when anodic hafnium oxide is formed by cross migration of hafnium and oxygen ions is unique and has not been reported so far. The local consumption of hafnium to form hafnium oxide proceeds at a comparable rate with the oxidation of aluminum around the alumina cells. This implies that the current does not pass only through the growing nanoneedles, and the adjacent aluminum is consumed simultaneously with the development of the hafnium oxide nanoneedles until the aluminum is fully converted into its anodic oxide. The phenomenon is explained by the comparable ionic resistivities of the collection of hafnium oxide nanoneedles and the alumina barrier layer formed in the given electrolyte.

During the *re-anodizing* stage, the Hf layer is further oxidized, and new portion of rod-like oxide grows steadily within the pores. This process competes with the oxidation of hafnium layer at the hafnium-oxide/hafnium interface until neighboring concaved oxide areas merge and continue to grow as a relatively uniform bottom layer (Figure 9d). The relationship between these competing phenomena, influencing the development of the nanorods and thickening the bottom oxide layer, is mainly determined by the transport numbers for hafnium species. This is likely to be a complex value, also suggesting an outward migration of hafnium cations with oxidation states lower than 4+. The phenomenon is believed to result in the formation of amorphous hafnium suboxide (likely Hf_2O_3) in the needles (dominating amount) and rods (relatively smaller amount), which exists in equilibrium with the full oxide (HfO_2), both being amorphous. Unlike the upper film portion (the needles and rods), the bottom oxide grows polycrystalline at both the anodizing and re-anodizing stages (Figure 9d).

At the re-anodizing stage, as the voltage rises the population density of the hafnium-oxide nanoroots does not seem to change much. Thus the barrier layer is converted into a mesh whose holes are filled with the lower resistivity anodic hafnium oxide. Thereafter, the anodizing current flows preferentially, or solely through the nanoholes, and the remaining alumina in the mesh (barrier layer) is almost completely separated from the anodizing process. This continues until an electric breakdown interrupts normal oxide growth, which develops at voltages exceeding 400 V under the given anodizing conditions. Another feature in the system is the distribution of phosphorus. The phosphorus species are well identified within the root area and right under the roots (Figure 8e). As the size and configuration of the P-containing domains fit well the areas where the bottom hafnium oxide forms at the anodization stage, it is suggested that incorporation of phosphorus-containing species is due to the electrolyte-

derived ions that migrate inwards under the high electric field already at the anodizing stage and then may move even deeper during the re-anodizing stage, not reaching however the HfO_2/Hf interface because of their lower migration rate compared with O^{2-} or OH^- ions.³⁸

The presence of Al_2O_3 in the film composition also deserves an attention. In a small concentration, alumina is found already in the PAA-free anodized sample. This implies that Al_2O_3 is incorporated in the hafnium-oxide nanoroots. The surface concentration of Al_2O_3 becomes relatively higher in the re-anodized sample, and the alumina is present in the outer layer of the oxide nanorods, being mixed with the hafnium oxide to a depth of about 25 nm from the nanorods surface. This may be most realistically explained by the penetration of the outer layer of the alumina cell walls by the growing hafnium-oxide nanorods, in the way described elsewhere.^{10,11} To explain the presence of Al_2O_3 in the oxide nanoneedles, a reference is made to an early work by Habazaki and co-workers,³³ who studied anodic film growth on Al-Hf alloys in electrolytes giving compact anodic films. It is likely that, in the present case of the PAA-assisted anodization, the needles of hafnium oxide within the alumina barrier layer grow not merely by the displacement process but develop mixed with a small portion of alumina that remains in the holes of the mesh described above. From the XPS quantitative evaluation, the Hf/Al ratio in the nanoneedles is ~ 25 . In the mixed $\text{Al}_2\text{O}_3\text{-HfO}_x$ metal oxide of such concentration, the transport number for Hf^{4+} is expected to be above zero.³³ Concurrently, the Hf^{3+} cations might also migrate in the mixed Al-Hf metal oxide, the transport number being undefined though. Even if the transport number for the hafnium species cannot be precisely determined, it is clear that the mixed-oxide nanochannels within the alumina barrier layer behave as the current pathways transporting the hafnium cations to the electrolyte/oxide interface, where a portion of amorphous hafnium oxide grows in the form of nanorods. Some of the transported cations migrate upwards mixing with alumina in the outer layer of the alumina cell walls while other cations take part in the formation of new and relatively pure amorphous hafnium oxide inside the alumina nanopores. It is not immediately obvious why the hafnium oxide grows also at the electrolyte/nanorod interface. It might be because of the following main differences from the commonly accepted mechanism for compact anodic hafnium oxide growth. At the electrolyte/oxide interface the oxide grows amorphous due to the high current densities and hence the very high electric fields, being confined in the alumina nanopores, where the oxide formation mechanism may differ substantially from the classical case. Presumably, the solid-state migration of hafnium and oxygen species is no longer the case; instead a substance like liquid or gel-like ceramic is shortly existing between the bulk solution and metal substrate, until the components solidify at the moment when the electric field is cut off.

The way how the bottom oxide forms seems relatively more certain since the oxide is nanocrystalline, being

mostly HfO_2 contaminated with PO_4^{3-} ions coordinated with hafnium ions, which develops due to the inward migration of O^{2-} (OH^-) ions without direct contact of the oxide with the electrolyte, believably quite in accord with the classical model.³⁹ The polycrystalline structure of the bottom oxide layer is likely the reason for tiny nanobubbles (Figure 7) to form at the alumina/bottom-layer interface owing to oxygen evolution resulting from oxidation of a portion of O^{2-} ions migrating inwards but not participating in the oxide formation. The bubbles of O_2 , as small as 10 nm, developed initially at the bottom of the alumina barrier layer, move outwards along the roots due to the viscous oxide flow, as described elsewhere. There has been no reports on such an event in normally grown anodic oxides or PAA-assisted metal oxides. Thus, the phenomenon may be either unique or still hidden for other PAA-assisted metal oxide nanofilms, since the present work has employed the best available analytical tools capable of exposing the nanosized voids in the metal-oxide nanostructures for direct observation.

4.2 The unique ionic transport. It is commonly accepted that the anodic films on Hf thicken due to migration of oxygen species toward the metal with new oxide material developing at the film/metal interface only.^{12,33} This means that the transport number for Hf^{4+} is nearly zero (0.05). This should also be the case of Al/Hf superimposed metal layers since the anodic hafnium oxide grows crystalline, without mixing with the upper amorphous anodic alumina, similarly to the case of Al/Zr bilayer.³⁴ However, in the present case, the cooperative ionic transport during the film growth is obviously more complex as the film grows nanostructured and is clearly divided into the amorphous upper rod-like oxide and the crystalline bottom oxide. Determination of the transport numbers during the re-anodizing is based on meeting the following conditions: First, the hafnium metal under the PAA film is re-anodized in the solution that chemically dissolves neither the alumina nor hafnia. Second, the formation of new oxide occurs at both the electrolyte/hafnium-oxide interface (nanorods' tops) and the hafnium-oxide/metal interface (nanorods' bottoms) due to outward migration of hafnium ions and inward migration of oxygen ions through the growing hafnium oxide together in the upper (root plus rods) and lower (nanorod bases) film layers. Further, the alumina- and phosphorus-containing species are relatively minor components of the film and can be neglected. Last, the oxide formation at the electrolyte/nanorod interface leads to filling the pores by the growing hafnium oxide while the oxide formation at the oxide/metal interface leads to nanorod bottoms expanding and merging in the continuous oxide layer beneath the alumina film. As the interface between the bottom and upper film layers is well defined (Figure 9d), it can probably be used as a "marker plane".¹⁰ Therefore, the transport number of oxygen ions, t_{O} , responsible for anodic oxide growth at the oxide/metal interface is defined as

$$t_{\text{O}} = V_{\text{bot}}/V_{\text{tot}} = V_{\text{bot}}/(V_{\text{bot}}+V_{\text{rod+root}}) \quad (1)$$

where V_{bot} is the volume of the bottom hafnium oxide, $V_{rod+root}$ is the volume of the nanostructured hafnium oxide including the roots and rods, V_{tot} is the total volume of hafnium oxide formed. Using equation (1), $t_O=0.55$ is estimated from the volumes of the corresponding oxide portions determined using the 3-D model of the oxide film developed with a computer-aided graphic program based on the numerous SEM images and measurements performed on the images with an image processing software. Complementing the oxygen ions, the transport number of hafnium cations is 0.45. Thus, the calculated transport number for cation is much higher than that reported elsewhere for anodic films grown on hafnium at room temperature (0.05). This discrepancy confirms that the ionic transport in the nanostructured anodic hafnium oxide proceeds in the unique way, with no parallels in the niche of compact anodic oxide formation on hafnium metal, even when covered by a layer of different valve metal including aluminum. As mentioned above, the transport number for hafnium species is obviously a composite value, i.e., an average value of Hf^{4+} and Hf^{3+} ions generated at the oxide/metal interface and migrating outwards under the given electrical and electrolytic conditions.

To finalize the understanding of the anodic oxide growth in the system, let us describe the effect of annealing on the re-anodized film. In the film treated at 600 °C in the air-abundant atmosphere, thermal oxidation occurs further consuming the Hf metal, accompanied by recrystallization of the film resulting in smaller HfO_2 nanocrystallites less preferentially oriented. Notably, the thermally grown and pre-existing HfO_2 nanocrystals are present in the bottom oxide layer only, whereas the needles and rods remain amorphous. The vacuum annealing reduces the whole film including the bottom oxide leading to the lowest oxidation state of Hf present in the roots, accompanied by the appearance of metallic Hf. However, the impact of the annealing in vacuum is most significant as it results in crystallization of the upper part of the film, including the roots and/or rods, but still revealing only the presence of HfO_2 oxide crystal phases, with no crystalline suboxides formed (or detected). Interestingly, the treatment does not affect much the microstructure and texture of the oxide phases. Apart from the temperature impact, the re-anodizing process itself gives rise to the second, orthorhombic HfO_2 phase additionally to the monoclinic HfO_2 developed already in the anodized sample. The last but not least, the present study suggests that the crystal structure of the precursor Hf metal film should impact the structure of PAA-assisted anodic film that forms on it, which may be the subject of a future work.

5. SUMMARY AND CONCLUSIONS

1. 3-D hafnium-oxide nanostructures have been synthesized via the high-current anodization of sputter-deposited Al/Hf metal layers. The film growth, achieved so far in phosphoric, malonic, and oxalic acid aqueous solutions at room temperature, proceeds in consecutive steps involving the high-speed formation of PAA layer,

the superfast local oxidation of the Hf underlayer through the alumina barrier layer, and lengthening the oxide within the alumina nanopores with the simultaneous growth of a relatively uniform hafnium-oxide layer buffering the alumina from the remaining hafnium metal.

2. The PAA-dissolved re-anodized film, typically formed in 0.2 mol·dm⁻³ H₃PO₄, consists of an array of upright-standing hafnium-oxide nanorods having needle-like wide-spread nanoroots anchored to the hafnium-oxide bottom layer. The rods have complex chemical composition involving amorphous HfO_2 , a suboxide (likely Hf_2O_3), and a minor amount of Al_2O_3 , while the nanoroots are mostly amorphous Hf_2O_3 . The bottom oxide layer is mainly nanocrystalline HfO_2 , also comprising phosphorus-containing electrolyte-derived species located beneath the rods.

3. The experimentally determined transport numbers for O^{2-} and Hf^{4+} ions, being respectively 0.55 and 0.45, ultimately prove that the hafnium oxide forms at both the film/metal and electrolyte/film interfaces, even in comparable portions, which is a unique situation in the field of anodic films on hafnium metal and, more generally, all polycrystalline anodic oxide films.

4. Annealing the re-anodized films in air at 600 °C results in further oxidation of Hf metal, recrystallization of the monoclinic and orthorhombic HfO_2 phases, altering the Hf^{4+}/Hf^{3+} ratio in different parts of the film, the roots and rods being still amorphous. The annealing in vacuum leads to a substantial reduction of part of the hafnium oxide, even to metallic state, with simultaneous partial crystallization of the oxide rods and/or roots.

The nanostructured 3-D morphology, graded chemical composition, crystallization, and phase transition behavior of the films are expected to significantly affect electron transport phenomena in the films, giving rise to dielectric, semiconducting, electron conducting, or combined properties and diverse functionalities.

ASSOCIATED CONTENT

Supporting Information. Calibration of XPS spectra, summary of XPS Hf 4f shifts, comparative anodizing behavior, details of XPS profiling analysis and relevant surface changes, details and summary of XRD evaluation, and comments on EDX maps. This material is available free of charge via the Internet at <http://pubs.acs.org>.

AUTHOR INFORMATION

Corresponding Author

* A. Mozalev. E-mail: alexander.mozalev@ceitec.vutbr.cz.

Author Contributions

The manuscript was written through contributions of all authors. / All authors have given approval to the final version of the manuscript.

Notes

The authors declare no competing financial interest.

ACKNOWLEDGMENT

Research leading to these results was supported by a grant from the Czech Science Foundation (GA ČR) no. 17-13732S. Part of the work was carried out with the support of CEITEC Nano Research Infrastructure (MEYS CR, 2016–2019). Eduard Llobet acknowledges the ICREA Academia Award. The authors wish to thank Zdenek Pytlíček of CEITEC BUT for his help with computer-aided modeling.

REFERENCES

- (1) Robertson, J. High Dielectric Constant Oxides, *Eur. Phys. J.: Appl. Phys.* **2004**, *28*, 265–291.
- (2) Choi, J. H.; Mao, Y.; Chang, J. P. Development of Hafnium Based High-*k* Materials—A Review. *Mater. Sci. Eng., R* **2011**, *72*, 97–136.
- (3) Hong, X.; Zou, K.; DaSilva, A. M.; Ahn, C. H.; Zhu, J. Integrating Functional Oxides with Graphene. *Solid State Commun.* **2012**, *152*, 1365–1374.
- (4) Ramana, C. V.; Vargas, M.; Lopez, G. A.; Noor-A-Alam, M.; Hernandez, M. J.; Rubio, E. J. Effect of Oxygen/Argon Gas Ratio on the Structure and Optical Properties of Sputter-deposited Nanocrystalline HfO₂ Thin Films. *Ceram. Int.* **2015**, *41*, 6187–6193.
- (5) Tirosh, E.; Markovich, G. Control of Defects and Magnetic Properties in Colloidal HfO₂ Nanorods. *Adv. Mater.* **2007**, *19*, 2608–2612.
- (6) Tsuchiya, H.; Schmuki, P. Self-organized High Aspect Ratio Porous Hafnium Oxide Prepared by Electrochemical Anodization. *Electrochem. Commun.* **2005**, *7*, 49–52.
- (7) Stępień, M.; Handzlik, P.; Fitzner, K. Synthesis of ZrO₂ Nanotubes in Inorganic and Organic Electrolytes by Anodic Oxidation of Zirconium. *J. Solid State Electrochem.* **2014**, *18*, 3081–3090.
- (8) Mozalev, A.; Sakairi, M.; Saeki, I.; Takahashi, H. Nucleation and Growth of the Nanostructured Anodic Oxides on Tantalum and Niobium Under the Porous Alumina Film. *Electrochim. Acta* **2003**, *48*, 3155–3170.
- (9) Li, F.; Zhang, L.; Metzger, R. M. On the Growth of Highly Ordered Pores in Anodized Aluminum Oxide. *Chem. Mater.* **1998**, *10*, 2470–2480.
- (10) Mozalev, A.; Vázquez, R. M.; Bittencourt, C.; Cossement, D.; Gispert-Guirado, F.; Llobet, E.; Habazaki, H. Formation-Structure-Properties of Niobium-oxide Nanocolumn Arrays via Self-organized Anodization of Sputter-deposited Aluminum-on-niobium Layers. *J. Mater. Chem. C* **2014**, *2*, 4847–4860.
- (11) Mozalev, A.; Khatko, V.; Bittencourt, C.; Hassel, A. W.; Gorokh, G.; Llobet, E.; Correig, X. Nanostructured Columnlike Tungsten Oxide Film by Anodizing Al/W/Ti Layers on Si. *Chem. Mater.* **2008**, *20*, 6482–6493.
- (12) Pringle, J. P. S. The Anodic Oxidation of Superimposed Metallic Layers: Theory. *Electrochim. Acta* **1980**, *25*, 1423–1437.
- (13) Mozalev, A.; Calavia, R.; Vázquez, R. M.; Gràcia, I.; Cané, C.; Correig, X.; Vilanova, X.; Gispert-Guirado, F.; Hubálek, J.; Llobet, E. MEMS-microhotplate-based Hydrogen Gas Sensor Utilizing the Nanostructured Porous-anodic-alumina-supported WO₃ Active Layer. *Int. J. Hydrogen Energy* **2013**, *38*, 8011–8021.
- (14) Bendova, M.; Gispert-Guirado, F.; Hassel, A. W.; Llobet, E.; Mozalev, A. Solar Water Splitting on Porous-alumina-assisted TiO₂-doped WO_x Nanorod Photoanodes: Paradoxes and Challenges. *Nano Energy* **2017**, *33*, 72–87.
- (15) Mozalev, A.; Bendova, M.; Gispert-Guirado, F.; Pytlíček, Z.; Llobet, E. Metal-substrate-supported Tungsten-oxide Nanoarrays via Porous-alumina-assisted Anodization: From Nanocolumns to Nanocapsules and Nanotubes. *J. Mater. Chem. A* **2016**, *4*, 8219–8232.
- (16) Biesinger, M. C.; Lau, L. W. M.; Gerson, A. R.; Smart, R. St. C. Resolving surface chemical states in XPS analysis of first row transition metals, oxides and hydroxides. *Appl. Surf. Sci.* **2010**, *257*, 887–898.
- (17) Rietveld, H. A Profile Refinement Method for Nuclear and Magnetic Structures. *J. Appl. Cryst.* **1969**, *2*, 65–71.
- (18) Balzar, D. Voigt-function Model in Diffraction Line-broadening Analysis in *Microstructure Analysis from Diffraction*. Snyder, A. R.; Bunge, H.; Fiala, J. (Eds.), International Union of Crystallography, 1999.
- (19) Hill, R.; Howard, C. Quantitative Phase Analysis from Neutron Powder Diffraction Data Using the Rietveld Method. *J. Appl. Crystallogr.* **1987**, *20*, 467–474.
- (20) Knörrschild, G.; Poznyak, A. A.; Karoza, A. G.; Mozalev, A. Effect of the Anodization Conditions on the Growth and Volume Expansion of Porous Alumina Films in Malonic Acid Electrolyte. *Surf. Coat. Technol.* **2015**, *275*, 17–25.
- (21) Mozalev, A.; Sakairi, M.; Takahashi, H.; Habazaki, H.; Hubálek, J. Nanostructured Anodic-alumina-based Dielectrics for High-frequency Integral Capacitors. *Thin Solid Films* **2014**, *550*, 486–494.
- (22) Sarganov, V.; Morgen, P.; Nielsen, J. C.; Gorokh, G.; Mozalev, A. Study of the Initial Stage of Aluminum Anodization in Malonic Acid Solution. *Electrochim. Acta* **1987**, *23*, 1125–1127.
- (23) Morant, C.; Galan, L.; Sanz, J. M. An XPS Study of the Initial Stages of Oxidation of Hafnium. *Surf. Interface Anal.* **1990**, *16*, 304–308.
- (24) Sammelseg, V.; Rammula, R.; Aarik, J.; Kikas, A.; Kooser, K.; Kaambre, T. XPS and AFM Investigation of Hafnium Dioxide Thin Films Prepared by Atomic Layer Deposition on Silicon. *J. Electron Spectrosc. Relat. Phenom.* **2007**, *156–158*, 150–154.
- (25) Ohtsu, N.; Tsuchiya, B.; Oku, M.; Shikama, T.; Wagatsuma, K. X-ray Photoelectron Spectroscopic Study on Initial Oxidation of Hafnium Hydride Fractured in an Ultra-high Vacuum. *Appl. Surf. Sci.* **2007**, *253*, 6844–6847.
- (26) Cosnier, V.; Olivier, M.; Theret, G.; Andre, B. HfO₂-SiO₂ Interface in PVD Coatings. *J. Vac. Sci. Technol., A* **2001**, *19*, 2267–2271.
- (27) Suzer, S.; Sayan, S.; Banaszak Holl, M. M.; Garfunkel, E.; Hussain, Z.; Hamdan, N. M. Soft X-ray Photoemission Studies of Hf Oxidation. *J. Vac. Sci. Technol., A* **2003**, *21*, 106–109.
- (28) <https://xpsimplified.com/elements/hafnium.php>
- (29) Siket, C. M.; Bendova, M.; Mardare, C. C.; Hubálek, J.; Bauer, S.; Hassel, A. W.; Mardare, A. I. Interfacial Oxide Formation during Anodization of Hafnium/Aluminium Superimposed Layers. *Electrochim. Acta* **2015**, *178*, 344–352.
- (30) March, A. Mathematische Theorie der Regelung nach der Korngestalt bei affiner Deformation. *Z. Kristallogr.* **1932**, *80*, 285–297.
- (31) Dollase, W. Correction of Intensities for Preferred Orientation in Powder Diffraction: Application of the March Model. *J. Appl. Crystallogr.* **1986**, *19*, 267–272.
- (32) Takenaga, A.; Kikuchi, T.; Natsui, S.; Suzuki, R. O. Exploration for the Self-ordering of Porous Alumina Fabricated via Anodizing in Etidronic Acid. *Electrochim. Acta* **2016**, *211*, 515–523.
- (33) Fogazza, M.; Santamaria, M.; Di Quarto, F.; Garcia-Vergara, S. J.; Molchan, I.; Skeldon, P.; Thompson, G. E.; Habazaki, H. Formation of Anodic Films on Sputtering-deposited Al-Hf Alloys. *Electrochim. Acta* **2009**, *54*, 1070–1075.
- (34) Shimizu, K.; Kobayashi, K.; Skeldon, P.; Thompson, G. E.; Wood, G. C. Anodic Oxidation of Zirconium Covered with a Thin Layer of Aluminium. *Thin Solid Films* **1997**, *295*, 156–161.
- (35) Skeldon, P.; Shimizu, K.; Thompson, G. E.; Wood, G. C. Direct Observation of Anodic Film Growth on Superimposed

1 Aluminium and Tantalum Metallic Layers. *Philos. Mag. B* **1990**,
2 *61*, 927–938.

3 (36) Habazaki, H.; Skeldon, P.; Shimizu, K.; Thompson, G. E.;
4 Wood, G. C. Anodic Film Formation on a Sputter-deposited Al-
5 30at%Mo Alloy. *Corros. Sci.* **1995**, *37*, 1497–1509.

6 (37) Shimizu, K.; Habazaki, H.; Skeldon, P.; Thompson, G. E.;
7 Wood, G. C. Anodic Oxide Films on Valve Metals – Structure
8 and Properties. *J. Surf. Finish. Soc. Jpn.* **1999**, *50*, 2.

(38) Habazaki, H.; Shimizu, K.; Skeldon, P.; Thompson, G. E.;
Wood, G. C. The Behaviour of Iron during Anodic Oxidation of
Sputtering-deposited Al-Fe Alloys. *Corros. Sci.* **2001**, *43*, 1393–
1402.

(39) Wood, G. C. in *Oxides and Oxide Films*, Vol. 2, Diggle, J.
W. Editor, Marcell Dekker, New York, 1987, p. 41.

Tables

Table 1. Quantitative evaluation of TEM-EDX measurements on FIB-cut lamellas prepared from the re-anodized, vacuum-annealed, and air-annealed samples. A sub-stoichiometric $\text{Hf}^{n+}\text{O}_x(\text{PO}_4)_y$ compound is assumed to compose the anodic Hf-based oxides, whereas evaluation of the TEM-EDX reveals the oxidation state of Hf ($n+$) and the amount of phosphate (y) in $\text{Hf}^{n+}\text{O}_x(\text{PO}_4)_y$ in the different areas of the film cross-sections, as marked-numbered in Figure 8a.

$\text{Hf}^{n+}\text{O}_x(\text{PO}_4)_y$	re-anodized sample		vacuum-annealed sample		air-annealed sample	
	n (Hf)	y (PO_4)	n (Hf)	y (PO_4)	n (Hf)	y (PO_4)
1: nanorods	3.1	0.23	3.1	0.24	2.1	0.24
2: nanoroots	2.9	0.31	2.1	0.29	4.1	0.31
3: bottom oxide – upper	3.5	0.16	2.7	0.14	3.5	0.11
4: bottom oxide – lower	3.4	0.01	2.6	0.01	2.4	0.01
5: metal	0.5	0	0.9	0	n/a	o(?)

Figure Captions

Figure 1. The voltage- and current-time responses during the anodizing followed by re-anodizing in $0.2 \text{ mol}\cdot\text{dm}^{-3} \text{ H}_3\text{PO}_4$ electrolyte of an Al(700 nm)/Hf(200 nm) bilayer system sputter-deposited on a SiO_2 -coated silicon wafer. The marked stages are I – nucleation and beginning of a steady-state growth of pores in the alumina layer, II – steady-state pore growth (at $\sim 160 \text{ V}$) during the anodizing, III – re-anodizing the Hf underlayer to 400 V , IV – potentiostatic polarization at 400 V (current decay).

Figure 2. SEM (a, b, e, g) cross-fractured and (c, d, f, h) surface views of anodic films grown on the Al/Hf bilayer in $0.2 \text{ mol}\cdot\text{dm}^{-3} \text{ H}_3\text{PO}_4$ electrolyte during the *anodizing* (up to 23 s, see Figure 1) – upper panel and *re-anodizing* (up to 36 s, Figure 1) – lower panel. Images shown in (b, c, d, g, h) were taken after the porous anodic alumina (PAA) layer had been dissolved away from the corresponding films. The arrow in image (d) points out the direction of progress in the film development from ~ 5 till 23 s (PAA dissolved afterwards).

Figure 3. SEM cross-fractured and surface views of anodic films grown on the Al/Hf bilayer in $0.2 \text{ mol}\cdot\text{dm}^{-3} \text{ H}_2\text{C}_2\text{O}_4$ electrolyte via (a, b, c) anodizing at 50 V followed by (d, e, f) re-anodizing to 400 V . Images shown in (b, c, e, f) were taken after the PAA layer had been dissolved away.

Figure 4. 3-D modeled views showing the main steps for forming the hafnium-oxide nanostructures: (a) sputter-deposition of an Al/Hf bilayer, (b) anodizing the Al layer to form a PAA film, (c, d) PAA-assisted anodizing of the Hf layer, (e) PAA-assisted high-voltage re-anodizing of the Hf layer to grow hafnium-oxide nanorods, (a'-e') selective dissolution of the Al or PAA layers.

Figure 5. Experimental and curve-fitted XP Hf 4f spectra of unspattered (a) initial Hf metal film, (b) PAA-free anodized film, (c) PAA-half-etched re-anodized film, (d) PAA-free re-anodized film, (e) nanorods-free re-anodized film representing the bottom oxide layer, (f) PAA-free vacuum-annealed re-anodized film, (g) PAA-free air-annealed re-anodized film; (h) O 1s-Hf 4s and Al 2p spectra of the sputter-cleaned PAA-free re-anodized sample. The air- (atmospheric pressure) and vacuum- (10^{-4} Pa) annealings were performed at $600 \text{ }^\circ\text{C}$ for 5 h. The lower panel shows atomic concentration profiles and outlines for the PAA-free (i) re-anodized and (j) anodized Ar-ion etched samples; (k) comparative Al 2p profiles for the two samples, considering $\text{at}\%(\text{Al}+\text{Hf})=100\%$.

Figure 6. Experimental (red circles), calculated (black solid lines), and difference (grey lines underneath) diffractograms of the (a) anodized, (b) re-anodized, (c) air-annealed, and (d) vacuum-annealed hafnium-oxide nanofilms.

Figure 7. Selected TEM images of a FIB-cut lamella prepared from the re-anodized sample showing (a) a group of three nanorods in the alumina pores where the roots, bottom oxide layer, and Hf metal are seen; (b) a zoomed-in nanoroot area where the bubbles/voids are clearly visible; (c) a fragment of the root/bottom-oxide interface imaged with higher resolution where the amorphous nature of the roots (FFT pattern in (d)) and densely packed nanocrystallites in the bottom oxide layer (FFT pattern in (e)) are displayed (the inset in panel (c) shows the place at a lower magnification); (f) a zoomed-in image of the border between the roots and bottom oxide where the crystal planes in the bottom oxide are visible.

Figure 8. (a) TEM image of a fragment of FIB-cut lamella of the re-anodized sample with marked areas where the quantitative analysis was performed (summarized in Table 1); (b-e) EDX elemental maps of the same area in the re-anodized sample showing at.% of Hf, O, Al, and P; (f, g) images combining TEM views with the corresponding EDX elemental maps (using the same color as coded in (b-e)) of the re-anodized and air-annealed samples, respectively.

Figure 9. Ionic transport and anodic oxide growth during the high-current PAA-assisted anodizing/re-anodizing of a thin layer of Hf (a) porous anodizing of the Al layer, (b) nucleation of anodic oxide on Hf underlayer, (c) development of amorphous hafnium-oxide nanoneedles with nanobubbles inside, (d) growth of amorphous mixed-oxide nanorods in the pores along with the formation of nanocrystalline HfO_2 bottom layer.

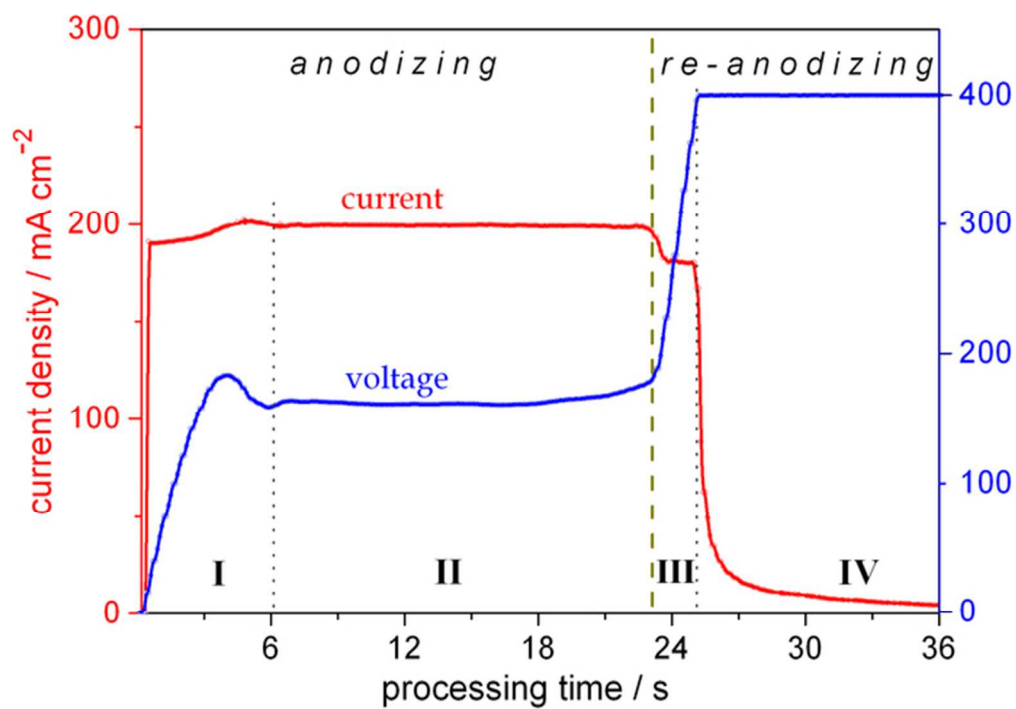


Figure 1

58x40mm (300 x 300 DPI)

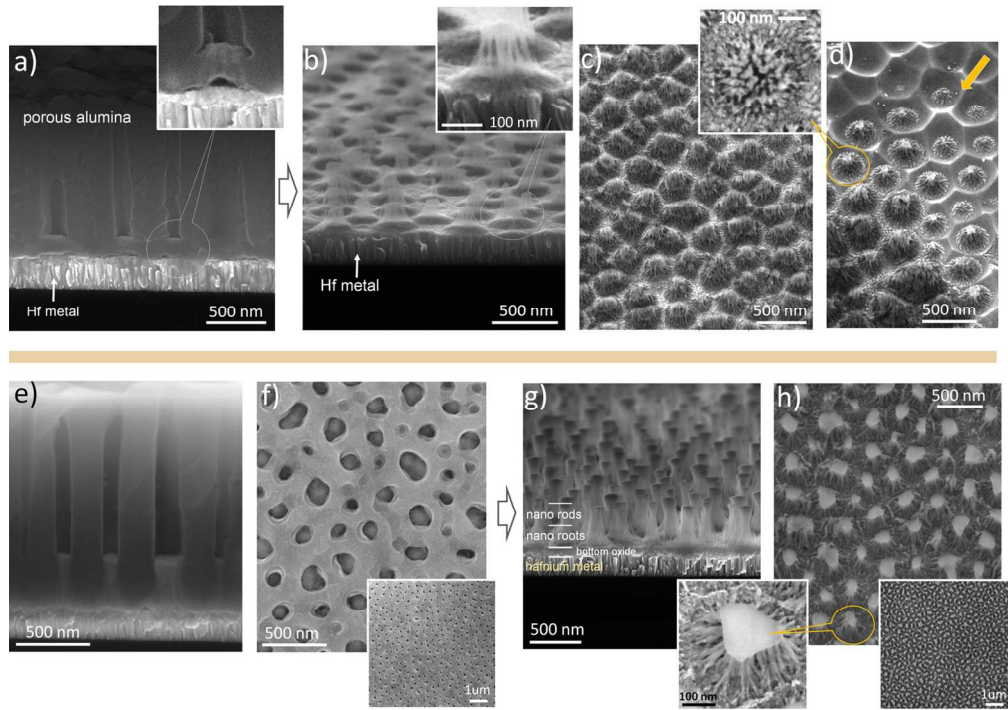


Figure 2

130x91mm (300 x 300 DPI)

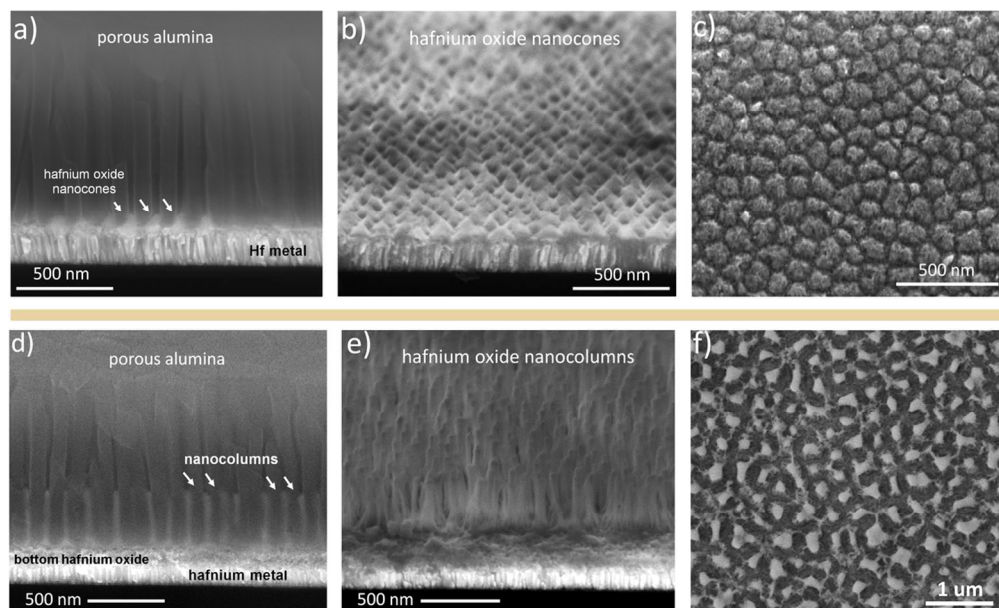


Figure 3

111x67mm (300 x 300 DPI)

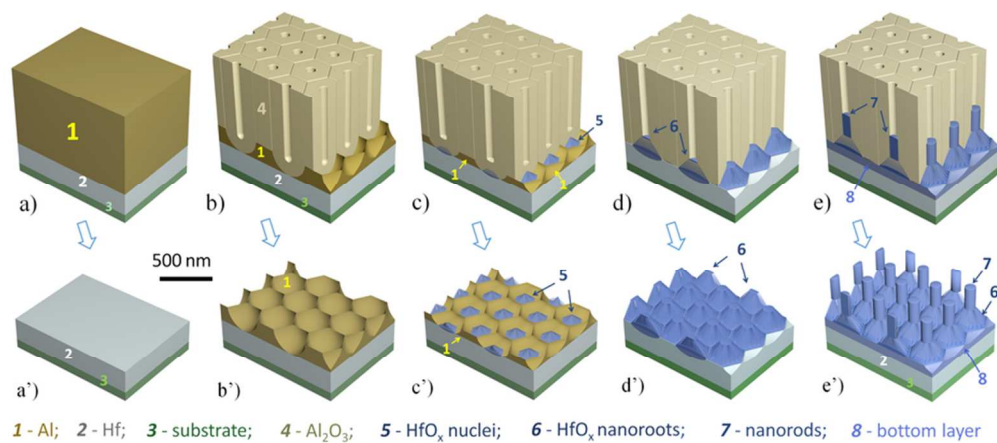


Figure 4

78x34mm (300 x 300 DPI)

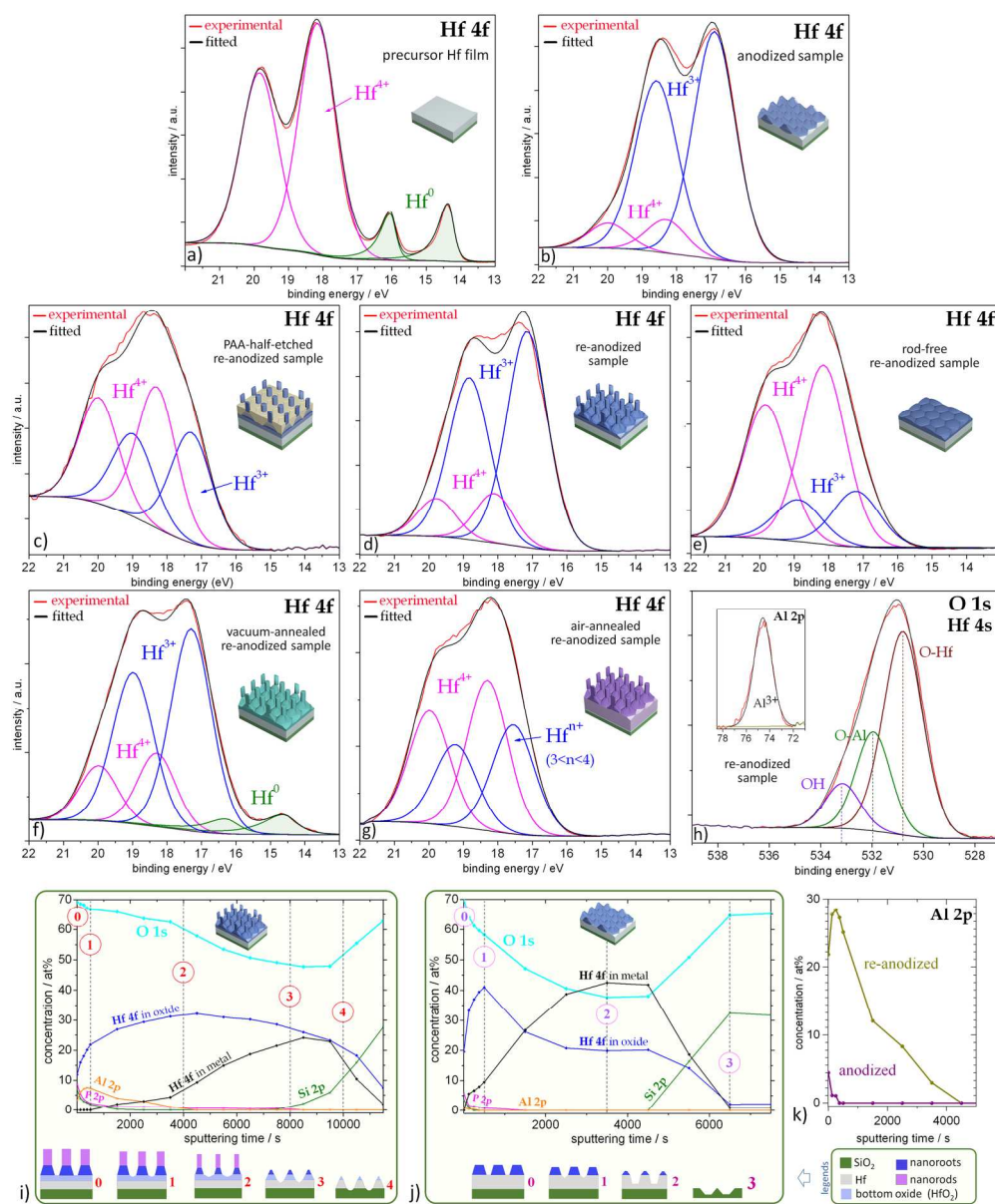
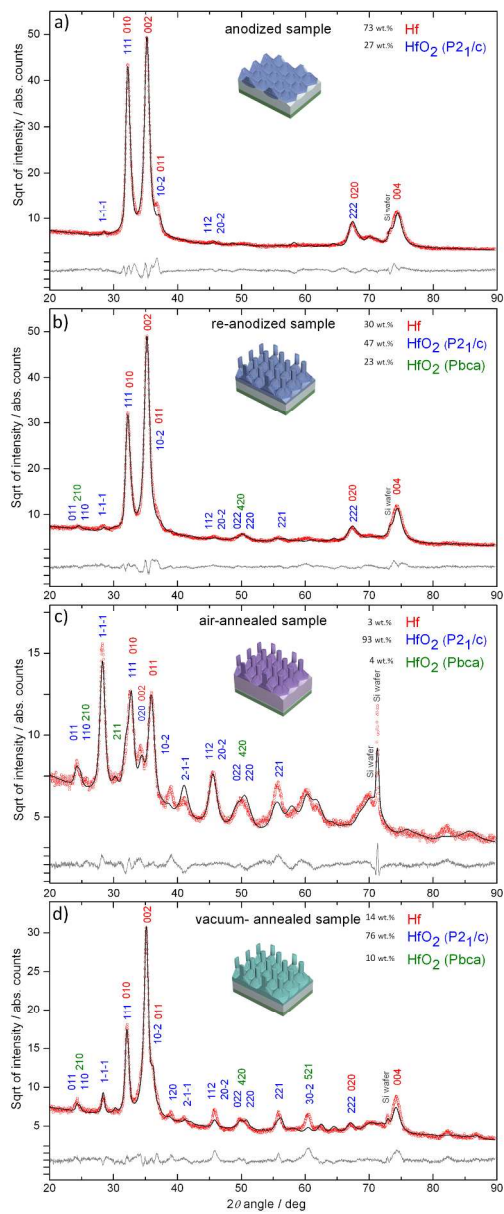


Figure 5

189x226mm (300 x 300 DPI)



202x493mm (300 x 300 DPI)

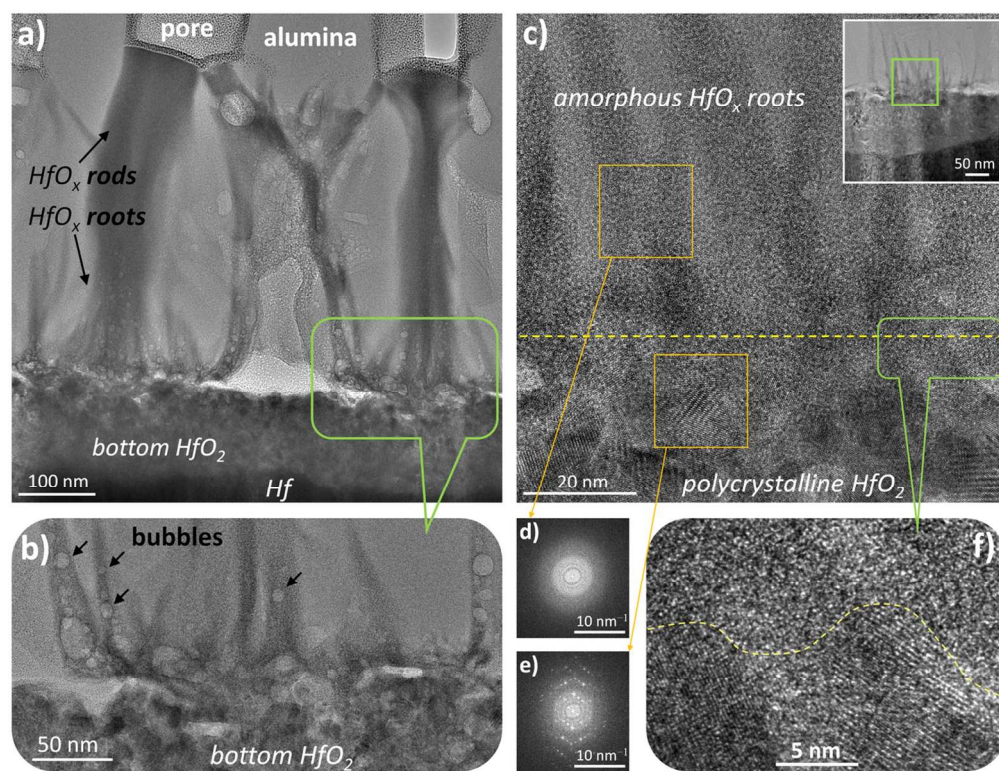


Figure 7

117x89mm (300 x 300 DPI)

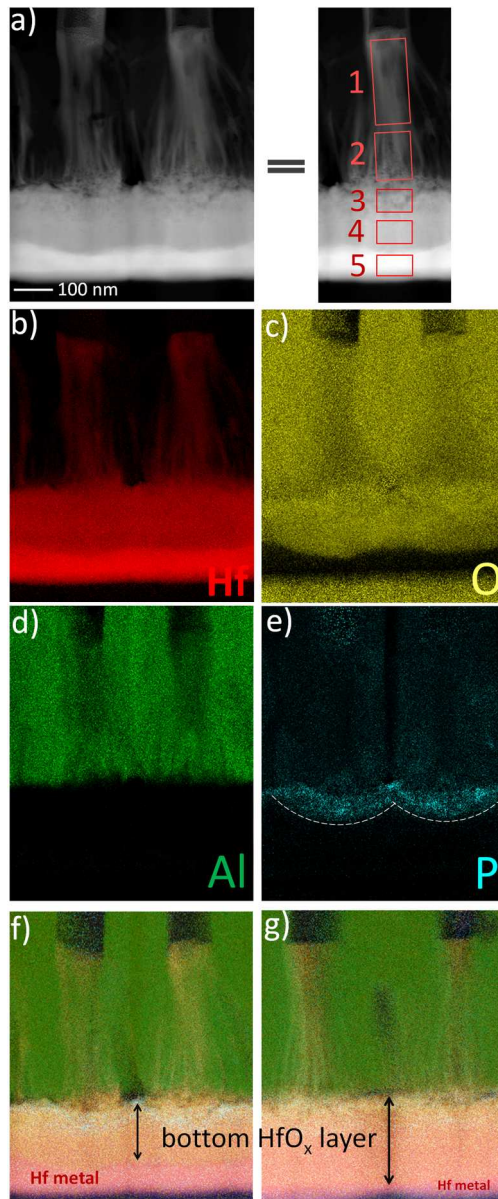


Figure 8

141x341mm (300 x 300 DPI)

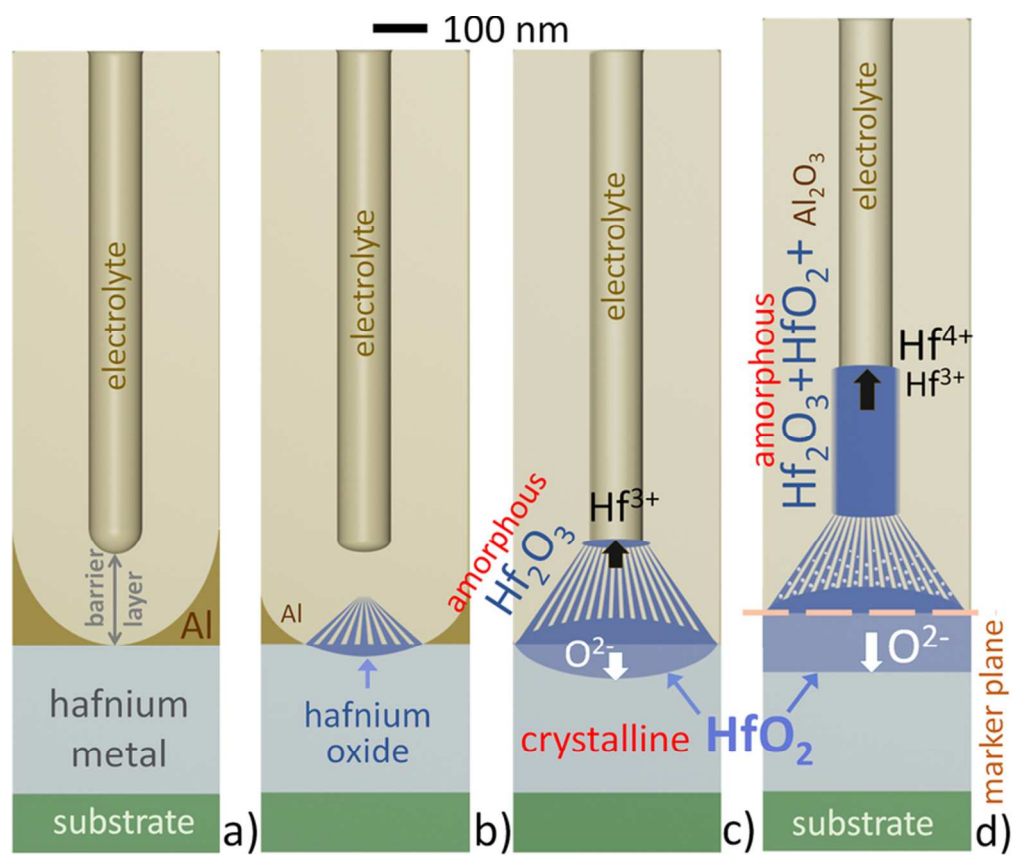
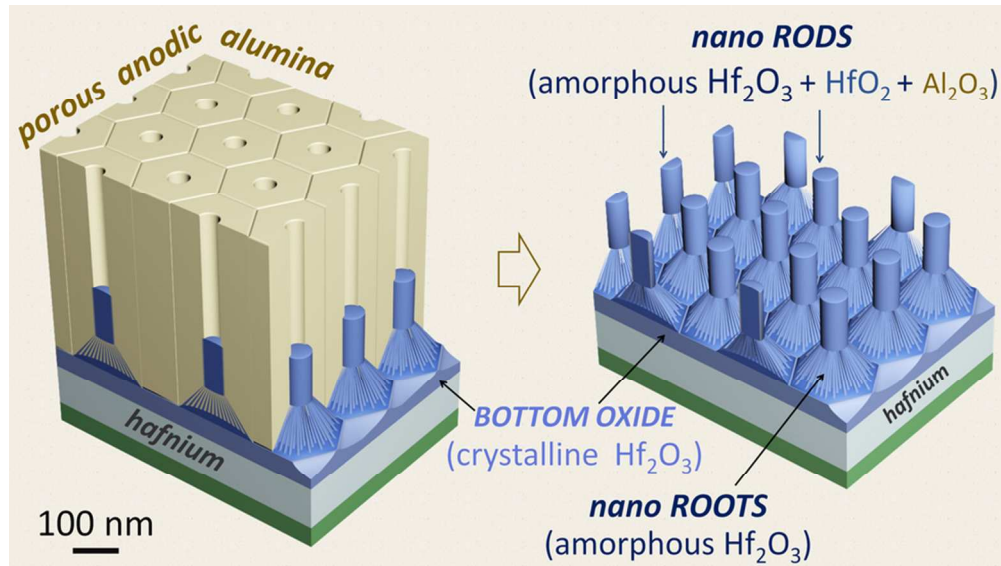


Figure 9

70x59mm (300 x 300 DPI)



TOC

82x46mm (300 x 300 DPI)